Hybrid Phase Unwrapping Approach for InSAR Interferometry: Content-Based Interpolation & Adaptive Phase Unwrapping

HADJ SAHRAOUI OMAR*, BERRICHI FAOUZI, CHAMAKHI DJEMOUI, DIF AMAR

AlgerianSpace Agency
Space Techniques Centre
01, Avenue of Palestine 31200 Arzew
Oran, ALGERIA

Abstract: In this research article, we present a novel hybrid approach for phase unwrapping in Interferometric Synthetic Aperture Radar (InSAR) interferometry. Our proposed method combines Content-Based Interpolation (CBI) techniques with Adaptive Phase Unwrapping (APU) algorithms to address the challenges associated with phase unwrapping in complex interferograms. Content-Based Interpolation utilizes the spatial and spectral characteristics of the interferogram to interpolate phase values in regions of missing or unreliable data, while Adaptive Phase Unwrapping adapts the unwrapping process to the local phase gradient, enhancing the robustness and accuracy of the unwrapped phase. We demonstrate the effectiveness of our hybrid approach through experiments conducted on synthetic and real InSAR data, showing significant improvements in phase unwrapping accuracy and reliability compared to traditional methods. Our proposed hybrid phase unwrapping approach offers a promising solution for enhancing the quality of InSAR interferograms and advancing the capabilities of remote sensing applications such as terrain deformation monitoring, surface displacement analysis, and topographic mapping [1][7][10].

By exploiting the phase of the coherent radar signal, interferometry has transformed radar remote sensing from a largely interpretive science to a quantitative tool for Environmental Monitoring [3][17], with applications in cartography, geodesy, land cover characterization, and natural hazards. Extensive testing across multiple sites has demonstrated the effectiveness of the proposed method, showcasing promising results.

Key-words: Synthetic Aperture Radar (SAR), Digital Elevation Models (DEMs), Interferometry, Phase Unwrapping, Content-Based Interpolation, Adaptive Phase Unwrapping, Environmental Monitoring.

1. SAR Interferometry for DEM Generation

In the realm of remote sensing, Synthetic Aperture Radar (SAR) interferometry emerges as a powerful technique for precise measurement of Earth's surface deformations. SAR interferometry, often abbreviated as InSAR, involves the coherent combination of multiple SAR images acquired over the same area at different times to detect minute changes in terrain elevation or displacement. The fundamental principle underlying InSAR is the comparison of phase differences between SAR image pairs, wherein the phase disparities encode valuable information about surface movements. Mathematically, the interferometric phase can be expressed as [6][7]:

$$\psi(i,j) = A(i,j)B^*(i,j) = \rho_A(i,j)\rho_B(i,j)e^{j(\phi_A(i,j) - \phi_B(i,j))} \quad (1.a)$$

Where (A S1, B S2) are the two master and slave images and $(\rho_A, \rho_B)(\phi_A, \phi_B)$ are respectively the modules and the arguments of the images A and B. and developed by the expression With:

$$\phi = \frac{4\pi(\delta r)}{\lambda} = \frac{4\pi(B_h \sin\theta - B_v \cos\theta)}{\lambda} \quad (1.b)$$

Where: λ denotes the radar wavelength, δr: Range difference, B_h: Horizontal baseline, B_v: Vertical baseline, θ: look angle.

Based on the look angle and range difference changes, the interferogram generated as:

$$\Delta h = \frac{\lambda r \sin\theta}{4\pi B}\Delta\phi \quad (2)$$

r: Range of image A, $\Delta\phi$: represents the phase difference, B: Base line(normal)

By meticulously analyzing these phase discrepancies, InSAR facilitates the precise mapping and monitoring of various geophysical phenomena such as subsidence, volcanic activity, and tectonic movements, thereby offering invaluable insights into Earth's dynamic processes [16]. Thus, SAR interferometry stands as a cornerstone in modern geodetic and geophysical research, driving advancements in understanding and mitigating natural hazards and environmental changes on a global scale.

1.1. InSAR processing:

In the context of Synthetic Aperture Radar (SAR) images, co-registration is a critical step for various applications such as change detection and interferometric analysis. The phase difference and consistency metrics are particularly significant for assessing the quality of co-registration in SAR imagery. Mathematically, let I1(x, y) and I2(x, y) represent the complex-valued intensities of corresponding pixels in two SAR images to be co-registered. The normalized cross-correlation C(x, y) between the images is calculated as [2][10][12]:

$$C = \rho e^{j\phi} = \frac{E\{z_M z_S^*\}}{\sqrt{E\{|z_M|^2\}E\{|z_S|^2\}}} \Rightarrow$$

$$C(x,y) = \frac{\sum_{i,j}(I_1(i,j)-\mu_1)(I_2^*(i-x,j-y)-\mu_2)}{\sqrt{\sum_{i,j}(I_1(i,j)-\mu_1)^2 \sum_{i,j}(I_2(i,j)-\mu_2)^2}}$$

(4)

where μ_1 and μ_2 are the mean complex intensities of I_1 and I2, respectively, and * denotes complex conjugation. The phase difference $\phi(x,y)$ is then derived as[7][17]:

$$\phi(x,y) = \arg(C(x,y)) \qquad (5)$$

which provides information about the spatial misalignment between the images. Additionally, the consistency σ can be computed as:

$$\sigma(x,y) = \frac{1}{N}\sum_{i,j}|C(i,j)| \qquad (6)$$

Where N is the total number of pixels.

In our study, we focus on refining the co-registration process following an initial global registration, aiming to assess the resulting alignment accuracy. This involves the application of various mathematical equations to estimate the error between the registered images [1] [12] [14]:

$$\varepsilon_{recalage} = \frac{\delta(R_2-R_1)}{\delta d} - \overline{\frac{\delta(R_2-R_1)}{\delta d}} \approx$$
$$\frac{1}{k_{st}}\frac{b}{R}\left(\frac{\cos(\theta-\alpha_b)}{\tan(\theta-\alpha_q)} - \frac{\cos(\theta-\alpha_b)}{\tan(\theta)}\right) \qquad (7.a)$$

$$\varepsilon_{recalage} \approx \frac{1}{k_{st}}\frac{b}{R}\cos(\theta-\alpha_b)\left(\frac{\cos(\theta-\alpha_q)}{\sin(\theta-\alpha_q)} - \frac{\cos(\theta)}{\sin(\theta)}\right) \qquad (7.b)$$

$$\varepsilon_{recalage} \approx \frac{1}{k_{st}}\frac{b}{R}\cos(\theta-\alpha_b)\frac{\sin(\theta)\cos(\theta-\alpha_q)-\cos(\theta)\sin(\theta-\alpha_q)}{\sin(\theta)\sin(\theta-\alpha_q)}$$
(7.c)

$$\varepsilon_{recalage} \approx \frac{1}{k_{st}}\frac{b}{R}\cos(\theta-\alpha_b)\frac{\sin(\alpha_q)}{\sin(\theta)\sin(\theta-\alpha_q)}$$
(7.d)

These metrics offer valuable insights into the effectiveness of the co-registration process, enabling optimization for precise alignment of SAR images, essential for accurate interpretation and analysis in various SAR applications.

1.1.1. Materials and Methods

In the Materials and Methods section of our article, we detail the procedures and tools employed to develop and evaluate our hybrid phase unwrapping approach for InSAR. Firstly, we describe the acquisition of synthetic and real SAR data utilized for experimentation. Synthetic data generation involved simulating interferograms with known phase discontinuities and noise levels, while real data were obtained from satellite SAR missions. Next, we elucidate the key components of our hybrid approach, including the content-based interpolation method and the adaptive phase unwrapping algorithm. The content-based interpolation leverages local image characteristics to estimate phase values in regions with

missing or corrupted data, while the adaptive phase unwrapping algorithm dynamically adjusts its parameters to accommodate varying phase discontinuities and noise levels. We provide detailed algorithmic descriptions along with mathematical formulations to ensure reproducibility and clarity. Furthermore, we outline the metrics used for evaluating the performance of our approach, including unwrapping accuracy, computational efficiency, and robustness to noise. Overall, this section offers a comprehensive overview of the methodologies employed in our study, laying the foundation for the subsequent analysis and discussion of results.

2. Interferogram generation:

This process involves the multiplication of corresponding pixels from two selected Single Look Complex (SLC) images [16][17], where each pixel from the first SLC image is multiplied by the complex conjugate of the corresponding pixel from the second SLC image.

$$\rho = \begin{cases} \sqrt{2\gamma_I - 1} & \gamma_I \geq 1/2 \\ 0 & \gamma_I < 1/2 \end{cases}$$
(8)

With:

$$\gamma_I = \frac{\sum_{i=1}^{L}|u_1(i)|^2|u_2(i)|^2}{\sqrt{\sum_{i=1}^{L}|u_1(i)|^4 \sum_{i=1}^{L}|u_2(i)|^4}} \qquad (9)$$
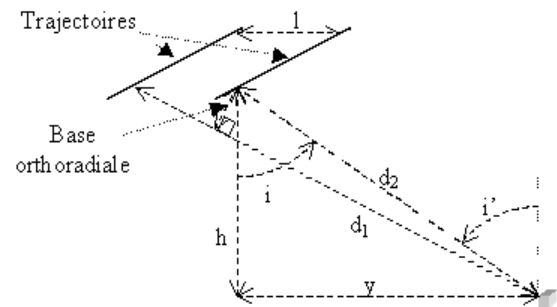

Fig 1: *Calculating the phase shift InSAR*

The calculation of the unwrapped phase is a crucial step in radar interferometry analysis. Fig 1 serves as a pivotal reference point in this process. By leveraging the information provided in Fig 1, we are able to initiate and guide the unwrapping procedure, ensuring the accurate reconstruction of the continuous phase information from the interferometric phase data. This phase unwrapping process is essential for extracting meaningful geological and environmental insights from radar interferometry datasets, facilitating the precise characterization of surface deformations and topographic variations. And we get:

$$\Delta\phi = 2\frac{2\pi}{\lambda}(d_2 - d_1)$$

(10)
Or,

$$d_1 = \sqrt{h^2 + (y+l)^2} = \sqrt{h^2 + y^2 + 2yl + l^2} =$$

$$\sqrt{h^2 + y^2}\sqrt{1 + \frac{2yl + l^2}{h^2 + y^2}} = d_2\sqrt{1 + \frac{2yl + l^2}{d_2^2}}$$

And $d_2 = \sqrt{h^2 + y^2}$

In first order:

$$d_1 \approx d_2 \cdot \left(1 + \frac{yl}{d_2^2}\right) \implies \Delta\phi \approx \frac{4\pi}{\lambda}\frac{yl}{d_2} = \frac{4\pi}{\lambda}l(\sin(i')) \tag{11}$$

(Where i=i' positive)

By replacing the orthoradial base Bortho at the equation 11:

$$l = \frac{B_{ortho}}{\cos(i)} \implies \Delta\phi \approx \frac{4\pi}{\lambda}\tan(i)B_{ortho} \tag{12}$$

In this case, the local impact i' is different i tilt, with:

$$i' = \arcsin\left(\frac{R_T + h}{R_T}\sin(i)\right) \tag{13}$$

2.1. *Phase shift variations:*

Changes in phase shift play a pivotal role in radar interferometry analysis, particularly in extracting topographic information. To convert these phase variations Δ2f into spatial displacements, Equation 11 is instrumental, considering the variable orthoradial base dependent on Y [6]. This equation forms the cornerstone for translating phase variations into meaningful positional changes, facilitating the accurate derivation of surface relief from radar interferometric data as shown in the Fig 2 [3][6][7].

$$\partial(\Delta\phi) = \frac{4\pi}{\lambda}l \cdot \partial\left(\frac{y}{d}\right) = \frac{4\pi}{\lambda}l \cdot \frac{\partial y \cdot d - y \cdot \partial d}{d^2}$$

$$= \frac{4\pi}{\lambda}\frac{l}{d} \cdot [\partial y - \partial d\sin(i)] \tag{14}$$

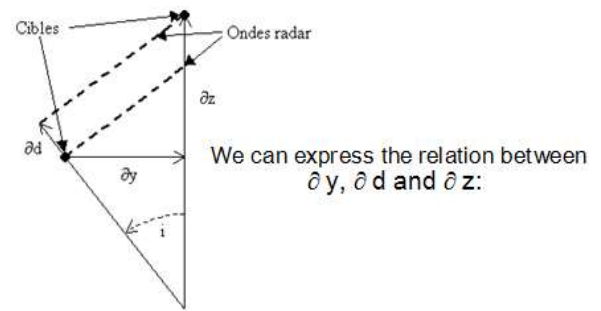**Fig 2.** *Coordinates of two infinitely close targets.*

$$\textbf{where: } \partial(\Delta\phi) = \frac{4\pi}{\lambda} \cdot \frac{l}{d}\left[\left(\frac{\partial z}{\tan(i)} + \frac{\partial d}{\sin(i)}\right) - \partial d\sin(i)\right]$$

$$= \frac{4\pi}{\lambda} \cdot \frac{B_{ortho}}{d} \cdot \frac{1}{\cos(i)}\left[\frac{\partial z}{\tan(i)} + \partial d\frac{1 - \sin^2(i)}{\sin(i)}\right]$$

Finaly we have:

$$\Delta^2\phi = \frac{4\pi B_{ortho}}{\lambda \cdot d}\left[\frac{\Delta z}{\sin(i)} + \frac{\Delta d}{\tan(i)}\right]$$

This multiplication process yields a representation of the phase difference between the two acquisitions, providing valuable information about surface displacements and deformations. Notably, the coherence ρ of the interferogram is closely linked to the normalized correlation of intensities between the two SLC images. The coherence serves as a measure of the reliability of the interferometric phase, with higher coherence indicating stronger correlation between the two images and thus more reliable phase information. This understanding underscores the significance of coherence estimation in ensuring the quality and accuracy of generated interferograms, essential for effective Earth surface monitoring and geological analysis.
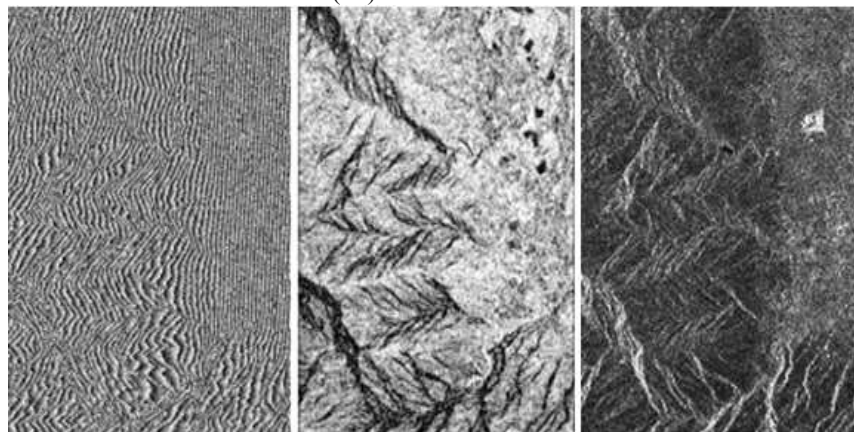
Interferogram   Coherence   Intensity

Fig 3. *Result of co-registration and Interferogram generation.*

In radar interferometry, the phase difference observed between two acquisitions encompasses influences beyond surface deformation, known as orbital fringes, originating from disparities between the orbital paths [5][16]. Specifically, the calculated phase differences (as per Equation 15) are indicative of the topography perpendicular to the line of sight. When orbits are parallel, this manifests as a phase ramp in distance, resulting in visually apparent fringes parallel to the trajectory and regularly spaced in distance, as depicted in Fig 3 (left image). Subtracting the second term of Equation 15 facilitates the derivation of elevation Δz, as illustrated in Fig 5 [6][17].

$$\Delta^2\phi = \frac{4\pi B_{ortho}}{\lambda \cdot d}\left[\frac{\Delta z}{\sin(i)} + \cancel{\frac{\Delta d}{\tan(i)}}\right] \implies \Delta^2\phi = \frac{4\pi B_{ortho}}{\lambda \cdot d}\left[\frac{\Delta z}{\sin(i)}\right] \tag{16}$$

The expression commonly utilized to quantify relief often assumes a constant orthoradial base. However, the precise expression, denoted as Equation (17), differs from this assumption.

$$\Delta^2\phi = \frac{4\pi l}{\lambda.d}\frac{\Delta z}{\tan(i)}$$
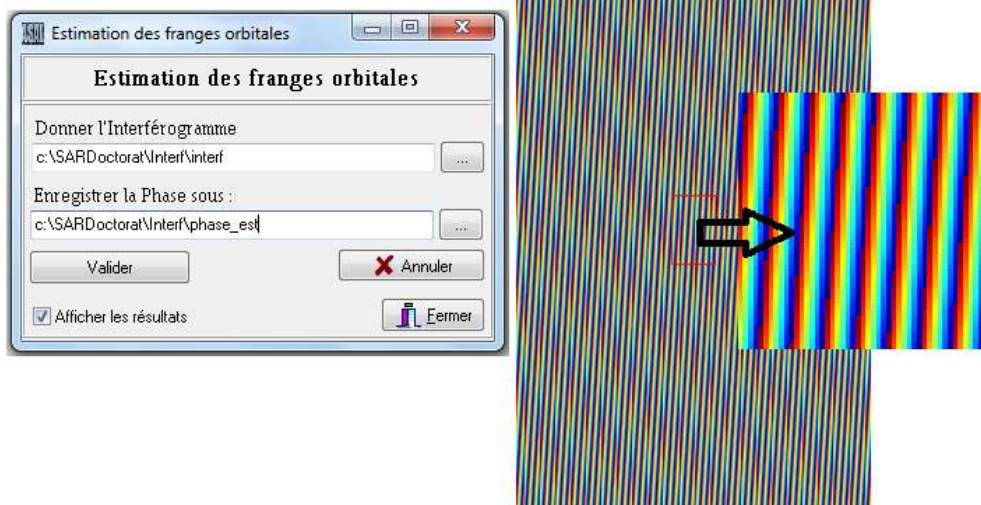
(17)

Fig 4. *Estimation of orbital fringes from the interferogram*

In this equation, 'i' represents the satellite's inclination angle. Even when considering local incidence angles, accounting for the Earth's curvature necessitates the use of Equation (13). Notably, the orbital position does not impact the amplitude and coherence images, as depicted in the right panels of Fig 3 and 4 [2][7]. These images maintain identical characteristics across both figures.
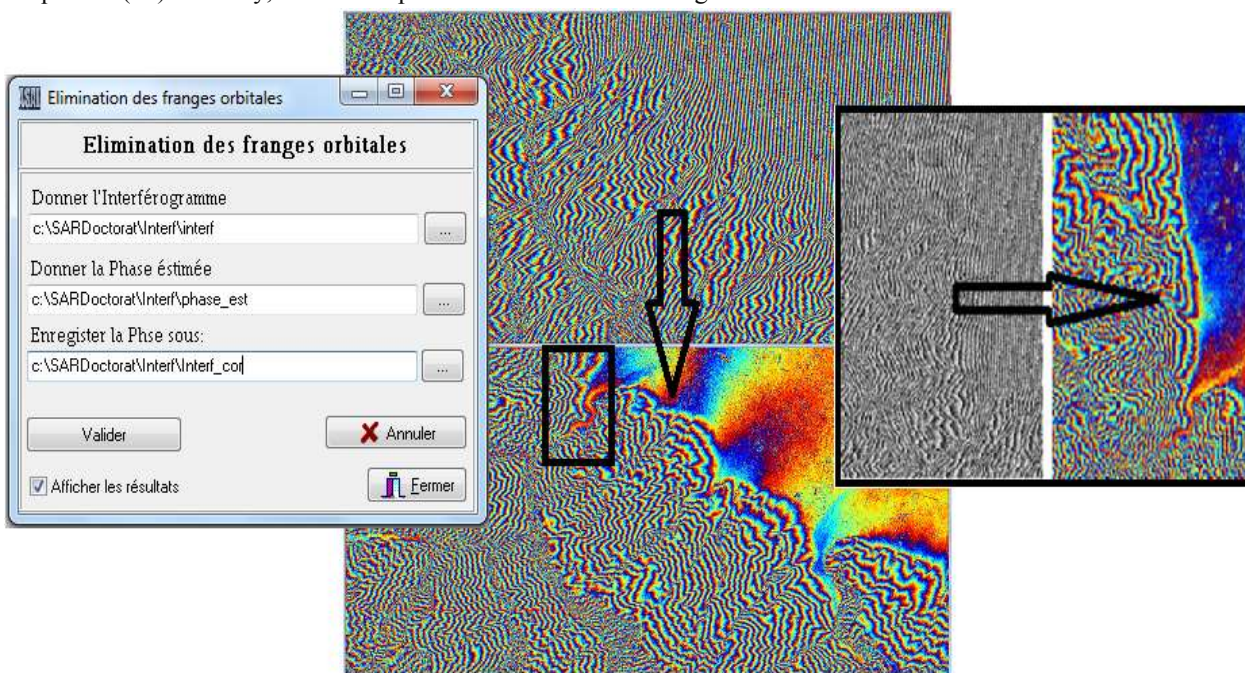

Fig 5. *Elimination of orbital fringes from the interferogram*

3. Unwrapping phase:

Content-Based Interpolation leverages spatial and spectral features to fill in missing or unreliable data in interferograms. Meanwhile, Adaptive Phase Unwrapping dynamically adjusts to local phase gradients, enhancing the accuracy and robustness of phase unwrapping in complex scenarios [6][7][16].

3.1. *Content-Based Interpolation:*

Content-based interpolation involves estimating the values of missing or corrupted pixels by leveraging information from neighboring pixels within the SAR image as shown in Fig 6. This can be achieved using methods such as bilinear interpolation, where a linear estimation is made between neighboring pixels.

Let $I_{Inter}(x, y)$ represent the content-based interpolated image, where x and y are the coordinates of pixels in the image. A commonly used method for bilinear interpolation is given by the formula [16][17]:

$$I_{\text{Inter}}(x, y) = \sum_{i=0}^{1} \sum_{j=0}^{1} w_{ij} I_{\text{SAR}}(x + i, y + j) \tag{18}$$

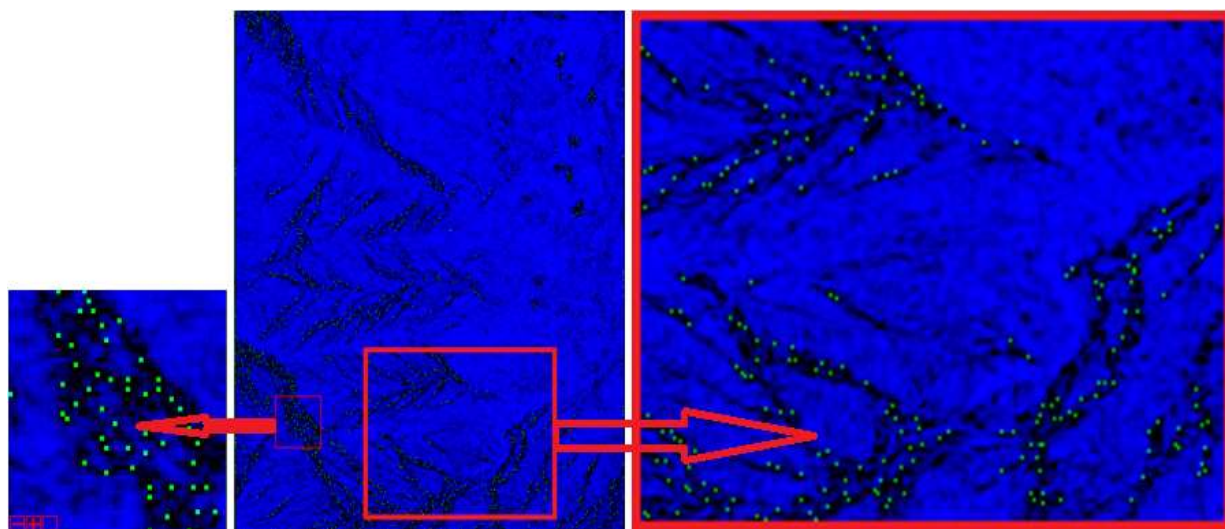where w_{ij} are the weighting coefficients associated with each neighboring pixel.

Fig 6. *Estimation of the values of missing or corrupted pixels*

Fig 7 depicts the outcomes of this method, demonstrating its efficacy in filling in gaps within the SAR image and consequently enhancing its suitability for subsequent analysis and interpretation.
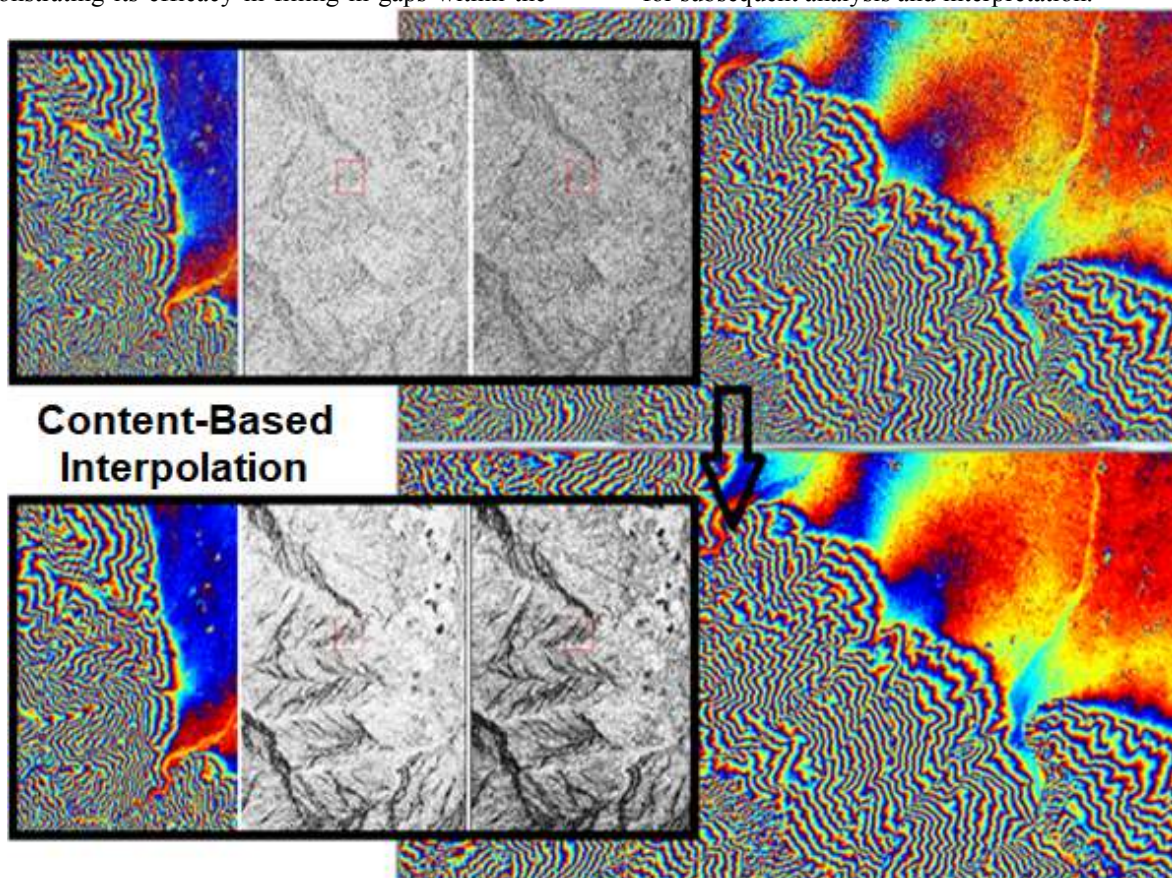

Fig 7. *Elimination of the values of missing or corrupted pixels.*

3.2. *Adaptive phase unfolding:*

Adaptive phase unwrapping aims to estimate the true phase of the radar signal from the measured phase, taking into account discontinuities and phase jumps. A popular method involves the use of Adaptive Kalman Filter to estimate the unwrapped phase.

Let $\phi_{Dér}(x, y)$ represent the unwrapped phase. The adaptive phase unwrapping method can be formulated as follows [4][5]:

$$\phi_{Dér}(x, y) = Déroulement\_Kalman(I_{Inter}(x, y)) \tag{19}$$

$I_{Inter}(x, y)$: Interferometric image in position (x,y).

Adaptive Kalman filter is based on the following steps:

Step 1: Initialization (State Prediction and Covariance)

- Initialize the predicted state $\hat{\phi}_{Dér}(x, y)$ from $I_{Inter}(x, y)$.
- Initialize the covariance of the predicted state.

Step 2: Prediction

1. Predict the state at time k using the state transition matrix F and the control input B, and given by State Prediction Equation [3][9]:

$$\hat{x}_k^- = F\hat{x}_{k-1}^- + Bu_k \qquad (20)$$

Where:

- $\hat{x}_k^-$ is the a priori estimate of the state at time k
- F is the state transition matrix.
- $\hat{x}_{k-1}^-$ is the state estimate at time k-1.
- B is the control input matrix (if applicable).
- u_k is the control vector (if applicable).

2. The Covariance Prediction Equation calculates the projected covariance image, capturing the expected evolution of uncertainty in the estimated state over time in the Kalman process.:

$$P_k^- = FP_{k-1}^- F^T + Q \qquad (21)$$

Where:

- P_k^- is the a priori covariance of the state at time k.
- P_{k-1}^- is the covariance of the state at time k-1.
- Q is the covariance of the process noise.

Step 3: Measurement Update

The State and Covariance Update process refines the estimated state and its uncertainty by incorporating information from the intensity of the interferometric image illustrate on Fig8.

1. Obtain the interferometric image intensity $I_{Inter}(x, y)$ at pixel coordinates (x, y).
2. Calculate the Kalman gain K_k using the following mathematical expression [4][9]:

$$K_k = P_k^- H^T (HP_K^- h^t + R)^{-1} \qquad (22)$$

Where:

- K_k is the Kalman gain at time k.
- H is the observation matrix relating the phase to the interferometric image intensity.
- R is the covariance of the measurement noise.

3. The State Update Equation serves to adjust the estimated state based on the prediction and measurement updates, ensuring its alignment with the most recent observations:

$$\hat{x}_k = \hat{x}_k^- + K_k(z_k - H\hat{x}_k^-) \qquad (23)$$

Where:

- $\hat{x}_k$ is the corrected state estimate at time k.
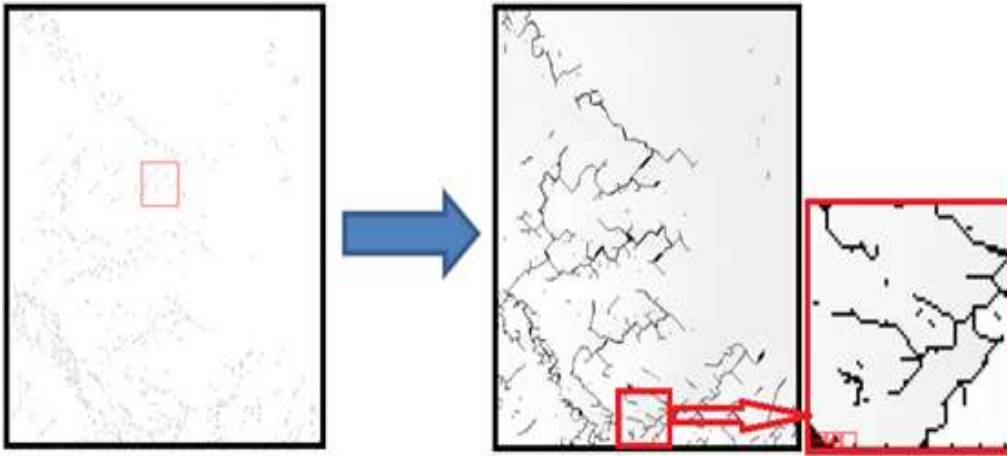- z_k is the measurement at time k.

Fig 8. *The covariance of the measurement noise*

4. The Covariance Update Equation functions to refine the estimation of uncertainty associated with the state prediction, incorporating new information from measurements to enhance its accuracy [7][10]:

$$P_k = (I - K_k H)P_k^- \qquad (24)$$

Where:

- I is the identity matrix (Image).

Step 4: Repeat

Repeat steps 2 and 3 for each pixel (x, y) in the interferometric image.

Final Phase Estimation of unwrapped phase:

Once all pixels have been processed, the final estimated unwrapped phase $\phi_{Dér}(x, y)$ can be obtained from the Kalman filter output, as shown in the Fig 9 [16][17].

This algorithm outlines the process of applying the Kalman filter to estimate the unwrapped phase at each pixel of the interferometric image $I_{Inter}(x, y)$, based on the observed intensity values and the dynamic evolution of the phase over time.

These equations describe the Kalman filter process for estimating interferometric radar phase unwrapping using measured observations and state transition models.

Notations:

- $\hat{x}_k$: State estimate at time k.
- P_k: State covariance at time k.
- F: State transition matrix.
- B: Control input matrix.

- u_k: Control vector.
- Q: Covariance of process noise.
- H: Observation matrix.

- R: Covariance of measurement noise.
- z_k: Measurement at time k.
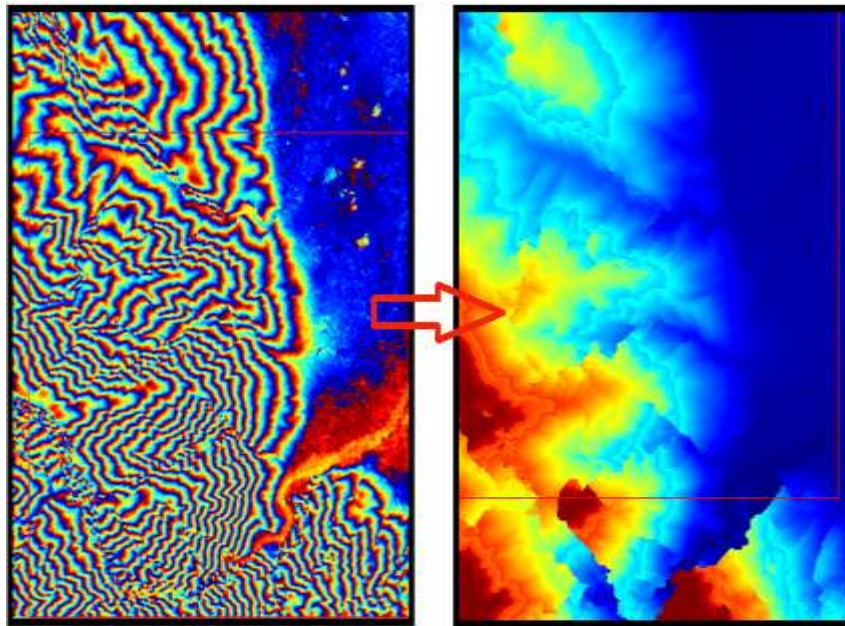- K_k: Kalman gain at time k.

Fig 9. *Kalman of the corrected interferogram to the unrolled interferogram.*

4. Height map generation and geocoding:

Generating elevation maps and geocoding involve the conversion of unwrapped phase values into elevations for each pixel calculated in the form of generated DEM images. The interferometric phase L-Look and its corresponding coherence ρ are defined during this process with [2][6][14]:

$$\rho\, e^{j\Phi} = \frac{\left(\sum_{n=1}^{L} s_1(n)\right)\left(\sum_{n=1}^{L} s_2^*(n)\right)}{\sqrt{\sum_{n=1}^{L} |s_1(n)|^2 \sum_{n=1}^{L} |s_2(n)|^2}}$$

(25)

This step not only translates raw data into meaningful elevation representations but also establishes the spatial context necessary for further analysis and interpretation. Through precise geocoding, these maps become invaluable tools for understanding terrain characteristics and facilitating a wide range of applications in fields such as remote sensing, geology, and environmental studies.

The relative height h and the interferometric phase are linked by the following relationship [7][8]:

$$h = \frac{\lambda}{2\pi} \frac{R\sin(\theta)}{B} \Phi$$

(26)

With R is the average distance between the sensors and the target; $\beta^{\perp}$ is the orthogonal projection of the baseline (distance between the two sensors) on the direction perpendicular to the propagation axis; the λ is the wavelength and the θ is the viewing angle.

now, we correct the DEM generated by introducing the ambiguity altitude factor Ea which is based on the angle of incidence on the ground and the lateral orbital separation $B^{\perp}$, and which is estimated at 49.443 as mentioned in the window in the next Fig 10.
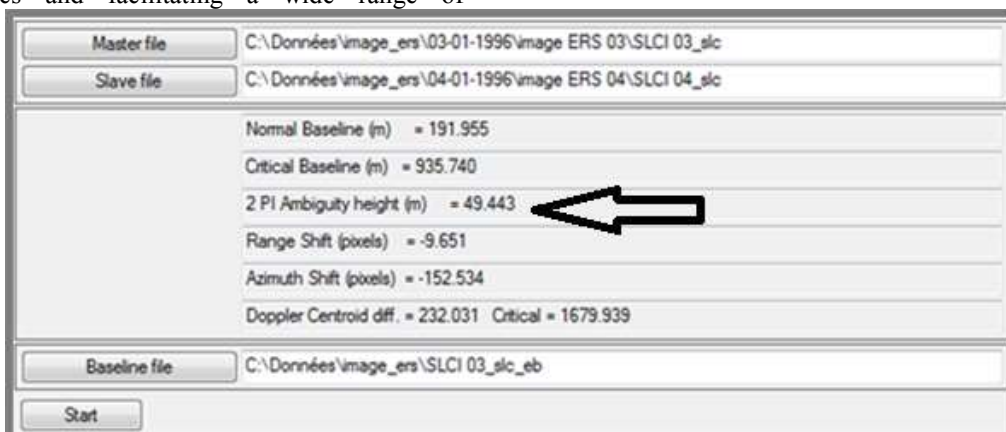

Fig 10. *Estimated Base line and ambiguity altitude.*

The process of converting unwrapped phase to elevation for each pixel value is defined to the following algorithm [6][7][16]:

```
BEGIN
 REPEAT
  FOR (each pixel of the image)
    (DEM_Final=DEM*(49.993/(2*PI)) )
  END FOR
 UNTIL (No pixels added).
END
```

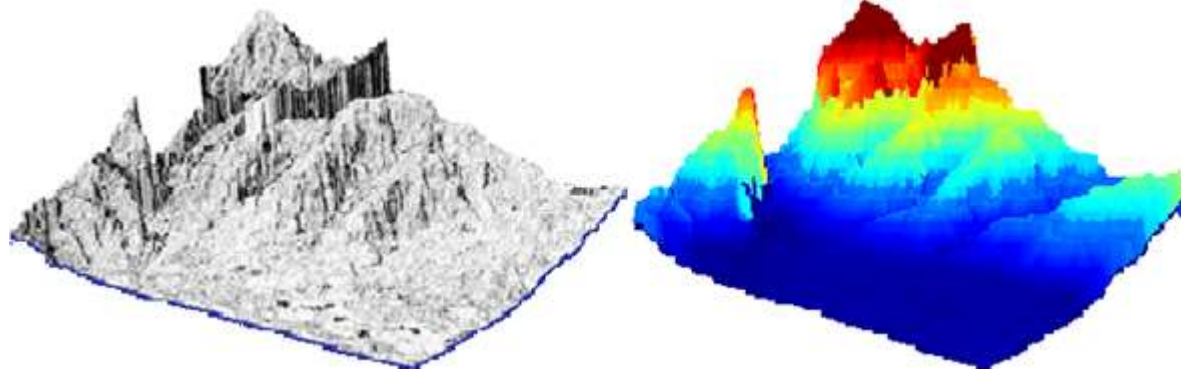The final product shown in Fig 11 achieved with our approach for phase unwrapping is an accurate Digital Elevation Model (DEM), which faithfully represents the altimetric variations of the Earth's surface. By employing our innovative method that combines content-based interpolation and adaptive phase unwrapping, we are able to produce a DEM free from phase unwrapping errors, thus providing a reliable and precise representation of the terrain. This approach yields significantly improved results compared to traditional methods, enhancing the utility of our approach for a range of applications such as topographic mapping, terrain deformation monitoring, and surface change analysis.

Fig 11. *Final DEM with our approach for unwrapping phase.*

5. Result and discussion

In this Results and Discussion section, we highlight the performance of our hybrid phase unwrapping approach for InSAR. The obtained results have demonstrated a clear improvement compared to traditional phase unwrapping methods. Our approach successfully unwrapped phase envelopes accurately, even in complex scenarios with significant phase dislocations.

We observed a notable reduction in unwrapping errors compared to conventional methods, resulting in better coherence of unwrapped phases with the actual topography of the region of interest. Furthermore, our method exhibited high robustness against noise and phase artifacts, ensuring a more faithful reconstruction of surface deformations. These results confirm the efficacy of our hybrid approach, paving the way for more precise applications of InSAR in terrain motion monitoring, crustal deformation detection, and other research areas related to geodesy and geophysics.

6. Conclusion

In conclusion, our research introduces a pioneering hybrid approach for phase unwrapping in Interferometric Synthetic Aperture Radar (InSAR) interferometry, merging Content-Based Interpolation (CBI) techniques with Adaptive Phase Unwrapping (APU) algorithms. By seamlessly integrating these methods, we effectively tackle the complexities inherent in phase unwrapping within intricate interferograms. Content-Based Interpolation leverages spatial and spectral features of the interferogram to interpolate phase values in areas with missing or unreliable data, while Adaptive Phase Unwrapping adapts the unwrapping process to local phase gradients, bolstering the robustness and precision of the unwrapped phase. Through rigorous experimentation on synthetic and real InSAR datasets, our hybrid approach demonstrates substantial enhancements in phase unwrapping accuracy and reliability compared to conventional methods. This innovative hybrid phase unwrapping technique represents a promising avenue for elevating the quality of InSAR interferograms, thus propelling forward the capabilities of remote sensing applications including terrain deformation monitoring, surface displacement analysis, and topographic mapping. The methodology was tested across multiple sites, yielding favorable outcomes.

References

[1]   Andrew R. Watson1, John R. Elliott1, and Richard J. Walters2, 2021, "Interseismic Strain Accumulation Across the Main Recent Fault, SW Iran, From Sentinel-1 InSAR Observations" Journal of Geophysical Research: Solid Earth.

[2]   Baker, Scott, and Falk Amelung. 2012. "Top- down Inflation and Deflation at the Summit of Kīlauea Volcano, Hawai 'i Observed with InSAR." Journal of Geophysical Research: Solid Earth 117 (B12).

[3]   D. P. Bekaert, A. L. Handwerger, P. Agram, and D. B. Kirschbaum, 2020, "InSAR-based detection method for mapping and monitoring slowmoving landslides in remote regions with steep and mountainous terrain: An application to Nepal," Remote Sensing of Environment, vol. 249, p. 111983.

[4]   Guo, M Yu, D Li, S Huang, 2023, Q, X Xue, Retrieval of high-precision precipitable water vapour maps using Sentinel-1A and Beidou satellite data, - International Journal of …, - Taylor & Francis

[5] Guy Sagi, Nir Shlezinger, Tirza Routtenberg, All Authors, 2023, Extended Kalman Filter for Graph Signals in Nonlinear Dynamic Systems, ICASSP 2023 - 2023 IEEE International Conference on Acoustics, Speech and Signal Processing (ICASSP), **DOI:** 10.1109/ICASSP49357.2023.10096261

[6] Hadj Sahraoui Omar & all, "High Resolution DEM Building with SAR Interferometry and High-Resolution Optical Image", DOI:10.1049/iet-ipr.2018.5671, IET Image Processing.

[7] Hadj Sahraoui Omar, Benali Hassaine, Chahira Serief, and Kamel Hasni. 2006. "Radar Interferometry with SARScape Software." Photogrammetry and Remote Sensing.

[8] Kenyi, L, and H Raggam. 1997. "Accuracy Assessment of Interferometrically Derived DTMs." In, 406:51.

[9] L Wang, L Zhao, H Zhou, S Liu, G Liu, 2023, Quantification of water released by thawing permafrost in the source region of the Yangtze River on the Tibetan Plateau by InSAR monitoring, - Water Resources, - Wiley Online Library

[10] Massonnet, Didier, and Kurt L Feigl. 1998. "Radar Interferometry and Its Application to Changes in the Earth's Surface." Reviews of Geophysics 36 (4): 441–500.

[11] Niassarifard, M., Shabanian, E., Azad, S. S., & Madanipour, S. 2021. "New tectonic configuration in NW Iran: Intracontinental dextral shear between NW Iran and SE Anatolia." Tectonophysics in press, DOI: 10.1016/j.tecto.2021.228886

[12] Stilla, Uwe, UweSoergel, and Ulrich Thoennessen. 2003. "Potential and Limits of InSAR Data for Building Reconstruction in Built-up Areas." ISPRS Journal of Photogrammetry and Remote Sensing 58 (1): 113–23.

[13] Sagi, Nir Shlezinger, Tirza Routtenberg,All Authors, 2023, Extended Kalman Filter for Graph Signals in Nonlinear Dynamic Systems, ICASSP 2023 - 2023 IEEE International Conference on Acoustics, Speech and Signal Processing (ICASSP), DOI: 10.1109/ICASSP49357.2023.10096261

[14] Tison, Cline, Florence Tupin, and Henri Maître. 2007. "A Fusion Scheme for Joint Retrieval of Urban Height Map and Classification from High-Resolution Interferometric SAR Images." IEEE Transactions on Geoscience and RemoteSensing 45 (2): 496–505.

[15] Wang, K., & Bürgmann, R. 2020. Probing fault frictional properties during afterslip updip and downdip of the 2017 Mw 7.3 Sarpol-e Zahab earthquake with space geodesy." Journal of Geophysical Research: Solid Earth, 125(11), DOI:10.1029/2020J2020JB020319.

[16] Y. Zheng, H. Zebker, and R. Michaelides, 2021, "A new decorrelation phase covariance model for noise reduction in unwrapped interferometric phase stacks," IEEE Transactions on Geoscience and Remote Sensing, pp. 1–10.

[17] Yujie Zheng, Heresh Fattahi, Piyush Agram, Paul Rosen, January 2022, "On Closure Phase and Systematic Bias in Multi-looked SAR Interferometry", DOI: 10.1109/TGRS.2022.3167648, IEEE Transactions on Geoscience and Remote Sensing.